Palaeogeography, Palaeoclimatology, Palaeoecology 674 (2025) 113003

Contents lists available at ScienceDirect

Palaeogeography, Palaeoclimatology, Palaeoecology

journal homepage: www.elsevier.com/locate/palaeo

Influence of sampling strategy, alignment method and growth morphology on the temporal contextualization of high-resolution geochemical data

Lukas Fröhlich, Qian Huang *, Bernd R. Schöne

Institute of Geosciences, University of Mainz, Johann-Joachim-Becher-Weg 21, 55128 Mainz, Germany

ARTICLE INFO

Editor: M. Elliot

Keywords:
Bivalves
Temporal alignment
Geochemistry
Proxies
Sclerochronology
Numerical modeling

ABSTRACT

High-resolution proxy reconstructions of physical and ecological variables in aquatic environments are commonly derived from biogenic archives such as bivalve shells. Interpretation of geochemical data measured in circular-shaped sample spots placed along shell cross-sections requires precise temporal alignment. The latter can be challenging, because differences in growth rate, morphology and sampling methods introduce biases to the reconstructed signals. This study systematically evaluates the impact of different sampling strategies and alignment methods on the reconstruction of environmental signals, i.e., temperature oscillations and phytoplankton blooms. Synthetic environmental signals and digital shell models of the bivalve *Arctica islandica* were used to numerically simulate how environmental variables are recorded during shell growth. A novel alignment method is presented, demonstrating significantly improved reconstruction accuracy when compared to traditional techniques. The new method enhances the reliability of proxy-based environmental reconstructions using biogenic archives and offers new insights into highly dynamic environmental signals such as phytoplankton blooms.

1. Introduction

The accretionary growth of biogenic carbonates, such as fish otoliths, corals and mollusks shells encode environmental signals as geochemical properties during growth (e.g., Peharda et al., 2021; Tzadik et al., 2017). If the periodicity of incremental growth is known, geochemical proxies (stable isotopes, element chemical properties etc.), can be contextualized temporally (e.g., Thébault et al., 2009). These sclerochronological analyses enable the high-resolution reconstruction of environmental conditions in the past, including seasonal to multi-decadal changes in temperature, salinity and primary production (e.g., Butler et al., 2013; Jolivet et al., 2015; Reynolds et al., 2022). Collecting the sample material generally requires the abrasion or ablation of the mineralized hard parts. A common practice is to mill or drill powder from calcium carbonates or to ablate material in-situ using a powerful laser for element chemical analyses. Usually, distinct marks remain on the sampled surface. Smaller samples generally produce higher resolution time-series. However, aligning such records is particularly challenging, because (1) the growth rate of organisms varies on seasonal timescales (Goodwin et al., 2001; Jones and Quitmyer, 1996), (2) the geometry of the growth patterns (increment shapes) can introduce bias produced by unevenly sampled material, (3) the size of the sample spots in relation to the corresponding increment widths varies throughout the ontogeny of the organism (see Goodwin et al., 2003; Goodwin et al., 2001). If the growth patterns, the shape of the growth increments and the sampling methods are not properly considered, temporal misalignments of geochemical samples can occur, leading to misinterpretations of the reconstructed environmental signals.

Herein, we evaluated the impact of sampling strategies and temporal alignment methods on the reconstruction of sub-annual environmental signals in relation to variable growth increment morphologies. We present a new approach for temporally aligning proxy data determined in biogenic hard parts (exemplarily in bivalve shells) to improve the accuracy of translating geochemical data from a distance- into a time-domain. We used the long-lived bivalve, *Arctica islandica*, given its legacy of providing long-term paleoclimate records (Butler et al., 2013; Jones, 1980; Marchitto et al., 2000; Wanamaker et al., 2008; Weidman and Jones, 1994) and high-resolution paleoenvironmental variables (Höche et al., 2023; Schöne et al., 2022a, 2022b; Schöne and Huang, 2021). The major challenge is to assess the accuracy of the reconstructed chronologies because either the environmental data are unavailable or provide a temporal resolution differing from that of the shell archive. To

* Corresponding author.
E-mail addresses: lufroehl@uni-mainz.de (L. Fröhlich), qhuang01@uni-mainz.de (Q. Huang), schoeneb@uni-mainz.de (B.R. Schöne).

https://doi.org/10.1016/j.palaeo.2025.113003
Received 21 July 2024; Received in revised form 7 January 2025; Accepted 2 May 2025
Available online 8 May 2025

overcome these uncertainties, we first generated synthetic data mimicking the environmental fluctuations of sea surface temperature (SST) and phytoplankton abundance. Then, we developed 2D digital shell models that numerically simulated the process of the time and growth rate-dependent incremental shell formation, based on empirical shell morphology and growth data of *A. islandica*. These digital models facilitated the numerical discretization of shell formation by splitting annual increments into numerous small, sub-annual microgrowth steps, each representing an equal time interval (hereafter referred to as microgrowth increments). Note that these microgrowth increments do not refer to internal or external forcings producing sub-annual increments, e.g., based on tides or circadian rhythms, but were defined by arbitrarily short time steps, a necessary approach to discretize the overall continuous process of shell formation. Given that the absolute timing of each growth step was defined, the underlying synthetic time-series were used to assign environmental signals to the microgrowth increments of the shell models. This approach simulated the process of recording environmental signals as geochemical properties into the shell. Since the underlying variable, the hypothetical geochemical response and the shell geometry were mathematically described, digital sampling experiments were performed to test different sampling strategies. By using different alignment methods, the reconstructed signals were then compared to synthetic environmental signals allowing to quantify the accuracy of the reconstructions. Although this study focused on bivalve shells, the principles derived herein can apply to a variety of other biogenic archives that grow on periodic bases and can help to improve future sclerochronological studies.

2. Material and methods

2.1. Digital shell models

The morphology of the outer shell layer (OSL) of *A. islandica* shells (NE Iceland; see Marali and Schöne, 2015) were modeled in two dimensions based on empirical data of three cross-sections (Shell A, Shell B and Shell C; Fig. 1). The shell modeling procedure can be described as follows. (1) Cross-sections of *A. islandica* that were immersed in Mutvei's solution (cf. Schöne et al., 2005) were digitalized (Fig. 1A to D) using a stereomicroscope (Zeiss Stemi 508) equipped to a DSLR camera (Canon EOS RP) and a Schott VisiLED MC1000 sectoral dark-field light source. The microscope images were digitally stacked (Microsoft Image Composite Editor) generating high-resolution composite images of the cross-sections. (2) Landmarks were then positioned along the clearly visible

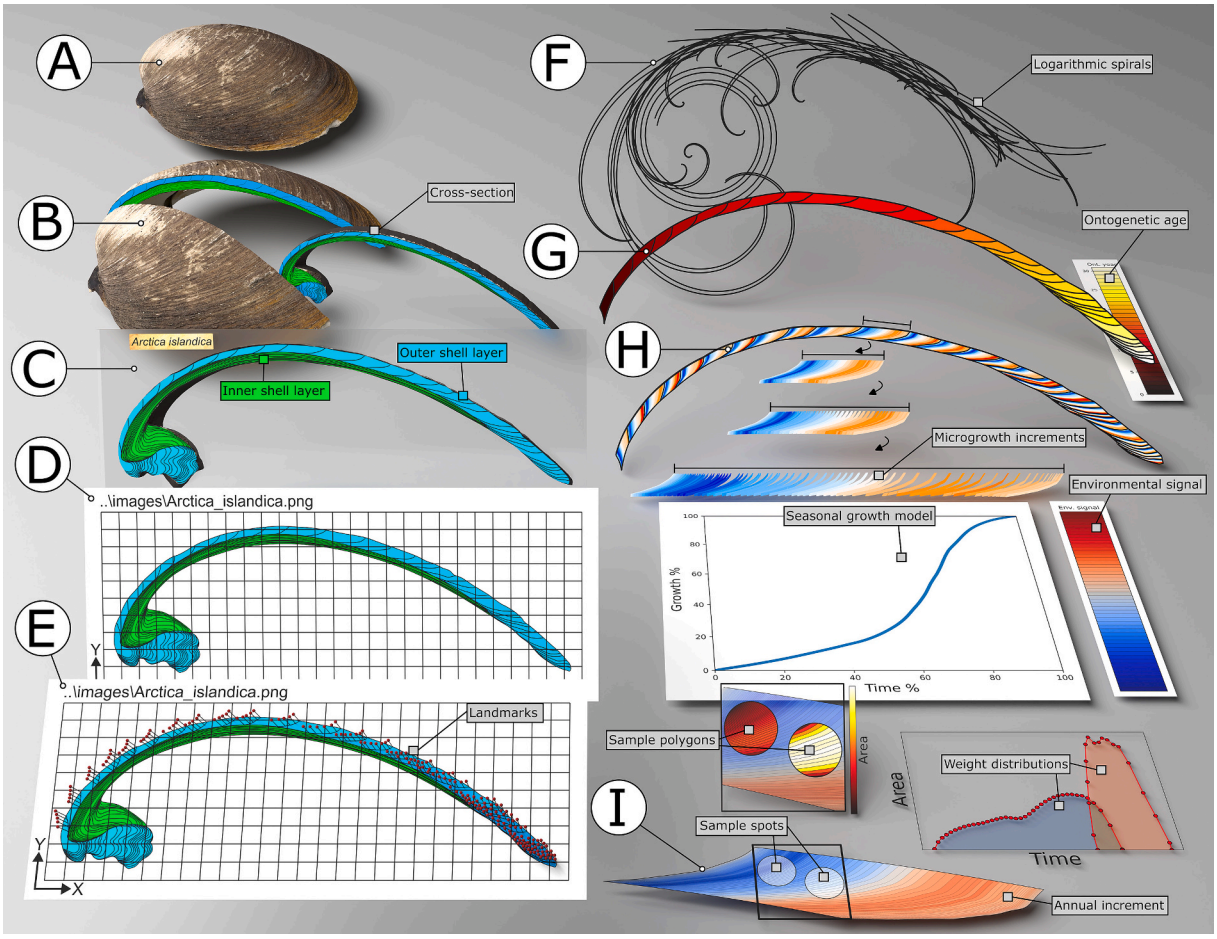

Fig. 1. Schematic illustration of the steps used to digitally construct shell cross-section. An *Arctica islandica* valve (A) was cut along the axis of maximum growth to obtain a several mm-thick cross-section (B). This cross-sectioned shell slab was then attached to a glass slide (C) and stained with Mutvei solution to enhance the visibility of the growth patterns. The cross-section was photographed with a digital camera (D) and landmarks (pixel coordinates) were positioned along the shapes of the annual growth lines (E), i.e., of the OSL. Logarithmic spirals were constructed according to the stacking increment model of Ubukata (2001) using the landmark coordinates (F). The spirals connected the inner and outer edges of each annual increment (G). Microgrowth increments were interpolated between the start and the end of annual growth lines following the inner and outer spirals (H). The width of the microgrowth increments were determined by the seasonal growth model and an underlying signal assigned to each growth increment. Two sample spots (indicated as circles) exemplarily positioned within an annual increment (I). As the microgrowth increments were numerically described, the area of an increment that is covered by a sample spot can be calculated and the weights of each microgrowth increment can be deduced. Although the two samples do not overlap spatially, there is a clear temporal overlap between them.

annual growth lines (Fig. 1E) and their pixel coordinates were retrieved. (3) Subsequently, the growth geometry for each annual increment was then digitally reconstructed according to the principles of the 'stacking increments model' presented by Ubukata (2001), which describes the accretionary shell growth of the outer shell layer as the result of 'stacking increments' where the geometry of a given increment determines the geometry and dimension of the successive increment (Supporting Information Fig. S1). To construct a stacking increments model, four growth parameters need to be defined (cf. Ubukata, 2001), namely, the ratio between the movement of the pallial line and the growth of the mantle (G); the ratio between the amount of deposited shell material at the outer edge and the growth of the mantle (C); the ratio between the amount of shell accretion at the pallial line (inner edge) and the growth of the mantle (C'); the magnitude of a given growth step (ε). At this stage, the growth fronts are represented by simple straight lines and can be represented by the vector $\overrightarrow{L}$ defined between two points P_1 and P_2 in Cartesian coordinates (Supporting Information Fig. S1), with the length of the growth front at time step s (L_s) defined as the magnitude of $\overrightarrow{L}$:

$$L_s = \left\|\overrightarrow{L}\right\| = \sqrt{(x_2 - x_1)^2 + (y_2 - y_1)^2} \tag{1}$$

with $\overrightarrow{P_1} = \begin{pmatrix} x_1 \\ y_1 \end{pmatrix}$, $\overrightarrow{P_2} = \begin{pmatrix} x_2 \\ y_2 \end{pmatrix}$. The remaining variables can be calculated by:

$$\varepsilon L_s G = \varepsilon \times L_s \times G,$$

$$\varepsilon L_s C = \varepsilon \times L_s \times C$$

(and)

$$\varepsilon L_s C' = \varepsilon \times L_s \times C' \tag{2}$$

The dimension of the successive growth front of the following discrete time step $s + \Delta s$ is then defined by

$$L_{s+\Delta s} = (1 + \varepsilon)L_s - \varepsilon L_s G \tag{3}$$

In the next step, the vector $\overrightarrow{L}$ is scaled to the length $\varepsilon L_s G$ to determine the position of P_G along the line segment P_1P_2. Similarly, the vector $\overrightarrow{L}_\perp$ perpendicular to $\overrightarrow{L}$ is scaled to $\varepsilon L_s C$ as well as to $\varepsilon L_s C'$ and anchored at, respectively, P_2 and P_G to calculate the position of both P_C and $P_{C'}$ (Supporting Information Fig. S1). Here, the position of $P_{C'}$ equals to the inner point of the newly generated growth front P_3. Finally, P_4 can be calculated as the end of a line segment with the length $L_{s+\Delta s}$starting at P_3 and intersecting P_C. The resulting points P_3 and P_4 describe the geometry of the growth front at $s + \Delta s$ and serve as new starting points for the following iteration, i.e., $P_{1s+\Delta s}$ and $P_{2s+\Delta s}$. If the growth parameters are constant, the shape of the stacking increments necessarily follows logarithmic spirals (Ubukata, 2001), allowing to calculate the spirals for the inner and outer edges (Fig. 1F and Supporting Information Fig. S1) of the OSL. In this study, a stacking increments model was constructed for each individual annual increment. Therefore, the growth parameters G, C, C' and ε had to be identified for each model. This was achieved by using the landmarks with known coordinates that were placed on digital microscope images of cross-sections positioned along annual growth lines (Supporting Information Fig. S2A). Since the stacking increments model generates straight instead of curved growth lines, the shape of the growth front was not considered at this stage but was addressed in a subsequent step (see below). Thus, the first and the last landmark of the growth lines served as the end points P_1, P_2, P_3 and P_4 of a given annual increment (Supporting Information Fig. S2B and C) from which the growth parameters were calculated. P_G was determined from $\overrightarrow{L}_\perp$ that intersects with $P_{C'}$ ($= P_3$) from which $\varepsilon L_s G$ and $\varepsilon L_s C'$ was calculated. Likewise, P_C was found as the intersection of $\overrightarrow{L}_\perp$ starting at P_2 and the line P_3P_4 allowing to determine $\varepsilon L_s C$. Additionally, $L_s$and $L_{s+\Delta s}$are defined as the magnitude of $\overrightarrow{P_1P_2}$ and $\overrightarrow{P_3P_4}$ (Fig. S2F). Finally, the increment-specific growth parameters were obtained by:

$$\varepsilon = \left(\frac{L_{s+\Delta s} + \varepsilon L_s G}{L_s}\right) - 1$$

$$G = \frac{\varepsilon L_s G}{\varepsilon \times L_s}, C = \frac{\varepsilon L_s C}{\varepsilon \times L_s} \text{ and } C' = \frac{\varepsilon L_s C'}{\varepsilon \times L_s} \tag{4}$$

According to these parameters, the stacking increments model was used to construct the logarithmic spirals that describe the outer and the inner edge of the respective annual increment (Supporting Information Fig. S3). The origin of the inner and outer spirals was numerically approximated by reverting the process of stacking increments model, i.e., calculating the geometry of the increment of a former instead of a successive time step, resulting in progressively smaller increments. Here, we iteratively minimized the Euclidean distance D between P_1 and P_2 to approximate the origin, so that

$$\lim_{n\to\infty} D_n = \lim_{n\to\infty} \left\|\overrightarrow{P_{2,n}} - \overrightarrow{P_{1,n}}\right\| \approx 0 \tag{5}$$

where $\overrightarrow{P_{1,n}}$ and $\overrightarrow{P_{2,n}}$ represent the position of P_1 and P_2 at iteration n. From this origin point, the radial distance r_1 and r_2 as well as the angles θ_1 and θ_2 were calculated (Supporting Information Fig. S3E and F). Given a logarithmic spiral defined in polar coordinates as

$$r = ae^{b\theta}, \tag{6}$$

the parameters a and b can be calculated using the angle difference (θ_Δ) between θ_1 and θ_2 (Fig. S3G):

$$b = \frac{ln\left(\frac{r_1}{r_2}\right)}{\theta_\Delta},$$

$$a = \frac{r_1}{e^{b\theta_1}} \tag{7}$$

depicting the scaling factor and the growth rate of the spiral, respectively. Accordingly, the inner and outer spirals can be constructed, with the start of the annual increment being defined by θ_1 and the end by θ_2 (Supporting Information Fig. S3H and I). Finally, the last steps generated the sub-annual microgrowth increments for each annual increment by taking their logarithmic growth into account (Supporting Information Fig. S4). Therefore, the landmarks of the annual growth lines were connected to the outer and inner spiral producing a closed polygon covering the entire annual increment (Supporting Information Fig. S4A). According to the seasonal growth model of *A. islandica* (taken from Höche et al., 2022), the percentage of shell growth was determined for each sub-annual time step (Supporting Information Fig. S4B). This allowed to resample the inner and outer spiral based on their arc lengths (between θ_1 and θ_2). Since the shape of the growth lines (i.e., start and end growth line of each increment) were described by heterogeneously distributed landmarks, a smoothing step was included (Supporting Information Fig. S4C). This was done by normalizing the growth lines, so that the first landmark is located at (0,0) and the last at (1,0) (Supporting Information Fig. S4C), enabling the equidistant resampling of those lines. Then, the start and end growth lines were smoothed by fitting cubic splines to the resampled points. These cubic splines were discretized equidistantly producing a sequence of points that were transformed back to their original position between the inner and the outer spirals (Supporting Information Fig. S4D). To generate a gradual transition from the inner spiral to the outer spiral, the parameters a and b were linearly interpolated, resulting in n intermediate logarithmic spirals that smoothly morphed between the inner and the outer spirals. These spirals were resampled according to their arc lengths and the seasonal growth model (Supporting Information Fig. S4E). The smoothed start and end growth lines were then cut into $n + 1$ segments

and equidistantly resampled (Supporting Information Fig. S4F and G). This resulted in pairs of segments, each containing an equal number of points, with segments on the starting growth line corresponding to segments on the ending growth line. By linearly interpolating the resampled points between a start segment and an end segment and position them between the two neighboring spirals, it was possible to generate clearly defined boundaries for the individual microgrowth increments that smoothly change their shape from the starting growth line, across the annual increment toward the end growth line (Supporting Information Fig. S4H and I).

This method allowed to numerically simulate the accretionary growth of *A. islandica* by discretizing the continuous growth into

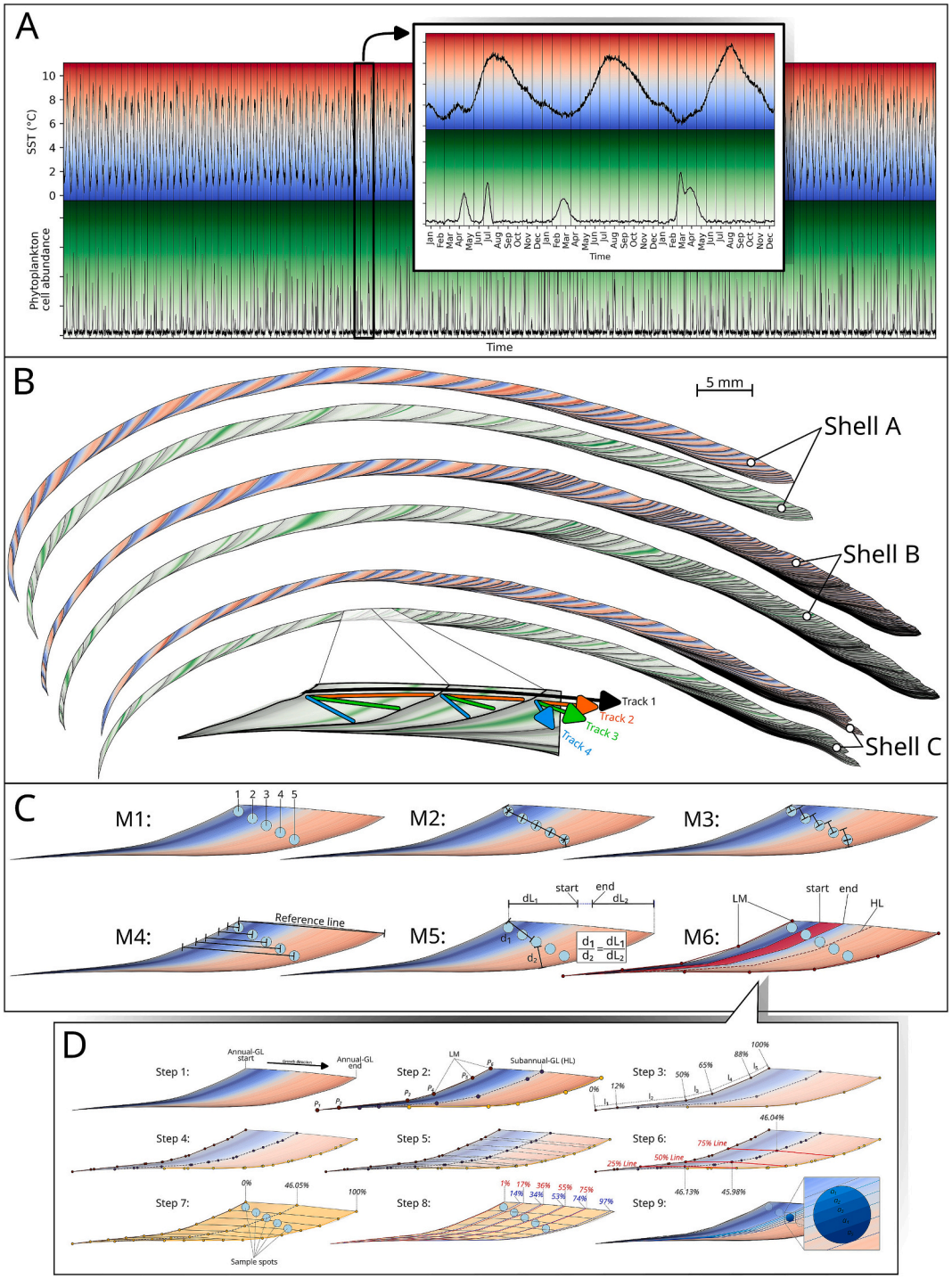

Fig. 2. Synthetically generated sea surface temperature (SST) and relative phytoplankton cell abundance time-series (A). Numerical models of the shell cross-sections (B) were constructed based on empirical data from the outer shell layer of three *Artica islandica* shells collected in northeast Iceland. Color variations in the shell models represent the environmental signals (from A) that were recorded in the shell during each moment of growth in the form of isochronous, subannual microgrowth increments. Tracks 1 to 4 schematically illustrate the relative positioning within the cross-sections of four different sampling tracks along which non-overlapping, digital sample spots (300 and 80 μm diameter) were placed. To temporally constrain each sampling spot, six different alignment methods were applied and tested (C). Panel D depicts the steps performed for alignment method 6 (M6). GL = growth lines; HL = helping lines; LM = landmarks. Information on the different alignment methods is provided in the Materials and Method section.

microgrowth steps. For the digital shell models, a resolution of 2000 microgrowth increments per annual increment was used. The geometry of each individual microgrowth increment was therefore represented as a two-dimensional polygon (see Fig. 1H, I), which enabled the digital resampling of specific shell portions to imitate the extraction of geochemical samples (Fig. 1I). The corresponding value, i.e., the geochemical signal measured, was then determined as the weighted sum of the values that were assigned to each microgrowth increment (Fig. 1I). The corresponding weights were determined by calculating the intersecting area between the microgrowth increments and the sample spot geometry, relative to the total area of the sample (Fig. 1I). As the microgrowth increments are temporally constrained, each sample spot obtained a unique time-dependent weight distribution (Fig. 1I). All calculations and statistics were performed using Python (3.12.3).

2.2. Synthetic environmental signals

Two environmental signals (SST and phytoplankton abundance; Fig. 2A) were generated to assign discretized values to individual microgrowth increments (see Section 2.1). These data were produced from randomly generated base signals with additional noise (e.g., Smith et al., 2023). The SST time-series (Fig. 2A) was based on monthly instrumental SST data from Iceland (Grímsey and Raufarhöfn; Hanna et al., 2006). An SST chronology was randomly generated using monthly averages, fitted with cubic splines and complemented with stochastic noise. The noise component was generated using the discrete Ornstein-Uhlenbeck differential equation aiming to imitate random environmental fluctuations (Smith et al., 2023). The dataset simulated a seasonally oscillating environmental signal. Conversely, the synthetic phytoplankton abundance (Fig. 2A) aimed to model individual blooms, as they can be reconstructed from barium-to-calcium ratios (e.g., Doré et al., 2020; Fröhlich et al., 2022; Marali et al., 2017; Schöne et al., 2023). Such profiles were characterized by variable peak magnitudes (between spring and summer) that episodically interrupt the constant background level (e.g., Gillikin et al., 2008). This behavior was modeled using Gaussian functions (Zhai et al., 2012), where the number of peaks (between 0 and 2), their timing (early spring to late summer), height, and width (5 to 20 days) were randomly determined. By generating 135 years of synthetic time-series, multiple environmental patterns were encompassed.

According to the formation time of the microgrowth increments, discretized signals were assigned to corresponding increments (Fig. 2B). This allowed to effectively imitate the incremental recording of environmental variables throughout shell growth. We assumed that (1) no time lag existed between the occurrence of the environmental signal and its encoding in the shell, (2) the archived values represent the corresponding environmental signals and (3) that the value assigned to a microgrowth increment is constant and does not change across its geometry.

2.3. Digital sampling experiments

Different digital sampling strategies were conducted to test how various positions of spots within an annual growth increment affect the accuracy of the signal reconstructions. The experiments differed by the direction of the sampling tracks that were used to equidistantly position sample spots (Supporting Information Fig. S5 to S7). Experiments 1 to 4 (abbreviated as Exp. 1 – Exp. 4) include sampling tracks (Fig. 2B) that were placed parallel to the outer shell surface (Exp. 1) to tracks that are almost perpendicular to the tangent of the direction of growth (Exp. 4). Criteria for positioning the samples were that spots do not overlap spatially and that a minimum of three samples fit into one annual increment. All experiments were performed using circular sample geometries with a diameter of 300 µm (i.e., a typical sampling resolution for $\delta^{18}O$ and $\delta^{13}C$ analyses; Trofimova et al., 2021) and 80 µm (i.e., a typical sampling resolution for element analyses; Fröhlich et al., 2023).

2.4. Temporal alignment methods

To compare the reconstructed signal with the underlying signal, the samples were temporally aligned using six different alignment methods (Fig. 2C; Table 1). For all these alignment methods, the sample spot positions within increments (i.e., growth percentage; %gr) were determined and translated into a temporal framework using a seasonal growth model for *A. islandica* (Höche et al., 2022). The alignment method 1 (M1) was based on the number of sample spots placed within an increment according to which corresponding %gr were calculated by dividing the respective growth increment into equally spaced steps (see Fig. 2C). Alignment method 2 (M2) involved digital image analysis to measure the distance between a spot center and a successive spot center as well as the shortest distance to the annual growth lines at the start and end for the first and last samples, respectively. Corresponding %gr then was calculated as the ratio between the cumulative distance to a spot center and the total length considering all segment distances. Alignment method 3 (M3) was also based on the distance between spot centers, but it involved calculations of the shortest distance between a hypothetical sub-annual growth line (visible or non-visible) intersecting a spot center and a subsequent spot center. Alignment method 4 (M4) was based on the shortest distance between a spot center and the annual start growth line. Then, this distance was related to the total width of the increment defined as the distance between the growth lines at the start and end as measured on the outer edge of the OSL. Alignment method 5 (M5) was modified after the procedure presented by Vihtakari et al. (2016). The measured shortest distances between the perimeter of a sample spot and the growth lines at the start (d_1) and end (d_2) were projected on a distance axis (i.e., the distance between the growth lines at the start and end) as dL_1 and dL_2 so that the ratio d_1/d_2 equaled dL_1/dL_2. This allowed to approximate a time interval covered by a sample spot, unlike M1-M4 which associate a sample spot to a single time value. Similarly, alignment method 6 (M6; Fig. 2D and Supporting Information Fig. S8), a novel approach developed in this study, approximated the start time and the end time covered by a sample spot. Briefly, this method is based on

Table 1
Overview and short descriptions of the alignment methods tested in this study. The principles of each alignment method are depicted in Fig. 2C and D.

Alignment method	Description	Features
M1	Equally sized growth steps determined by the number of sample spots within an increment.	Simple use, alignment of spot center, equidistant spacing assumed
M2	Shortest distance between successive spot centers and annual growth lines.	Distance measurements, alignment of spot center
M3	Shortest distance between spot center and sub-annual growth line intersecting preceding spot center.	Distance measurements, alignment of spot center, sub-annual growth line identification
M4	Distance between sample spots and annual growth line compared to the length of a reference line spanning from the annual start and end growth line.	Distance measurements, alignment of spot center, distances related to increment width
M5	Shortest distances of sample spot boundaries to annual start and end growth line projected onto a reference line.	Distance measurements, approximating time intervals covered by sample spots
M6	Growth increment morphology approximated. Annual and sub-annual growth lines digitally reconstructed using landmarks. Geometric interpolation steps used to estimate position and coverage of individual samples.	Digital image analysis required, increment shape considered using landmark coordinates, geometric operations required, temporal weight distributions approximated

nine steps. (1) The identification of annual growth lines and, if possible, sub-annual disturbance lines that act as helping lines (i.e., guidelines that help to describe the increment morphology). (2) The positioning of landmarks with known (pixel) coordinates along the growth lines to digitally capture the shape of the increments. (3) Each landmark is then converted into a percentage of the total growth line length based on the individual segments, i.e., the lines between successive landmarks. These percentages were stored and 25 %, 50 % and 75 % added. (4) Each growth line and helping lines is resampled (linear interpolation) according to the percentages, ensuring that each line contains knots with equal percentages. (5) As each growth line provide a similar number of knots, these landmarks can be connected between different growth lines producing lines spanning across the entire increment, i.e., connecting the start and end growth line. (6) If helping lines are used, the 25 %, 50 % and 75 % connection lines can be employed to determine at which percentage the helping line intersects these connection lines. Taking the mean percentage allows the approximation of the %gr that is represented by a helping line. Accordingly, a specific %gr can be assigned to each growth line (i.e., the starting growth line is 0 %gr, the ending growth line is 100 %gr, and each helping line falls between 0 %gr and 100 %gr). (7) The geometry and position of the sample spots is determined. (8) The connecting lines (see step 5) are then used as guidelines to linearly interpolate the shell growth at every %gr between the annual start and end growth line. For example, the growth line at 50 %gr can be reconstructed by finding the 50 %gr position on each connection line and by connecting these points with simple line segments. This step allows to approximate the start as well as the end %gr of a sample spot by taking the shape of the increment into account. (9) After the start and end gr% was defined, the corresponding %gr range can be subdivided into multiple slices using simple linear interpolation. This produces distinct polygons that intersect the entire sample spot. By calculating the area of the individual polygons within the sample spot (the sum of all polygon areas equals to the area of the sample spot), the relative contribution of each slice with a known %gr to the measured

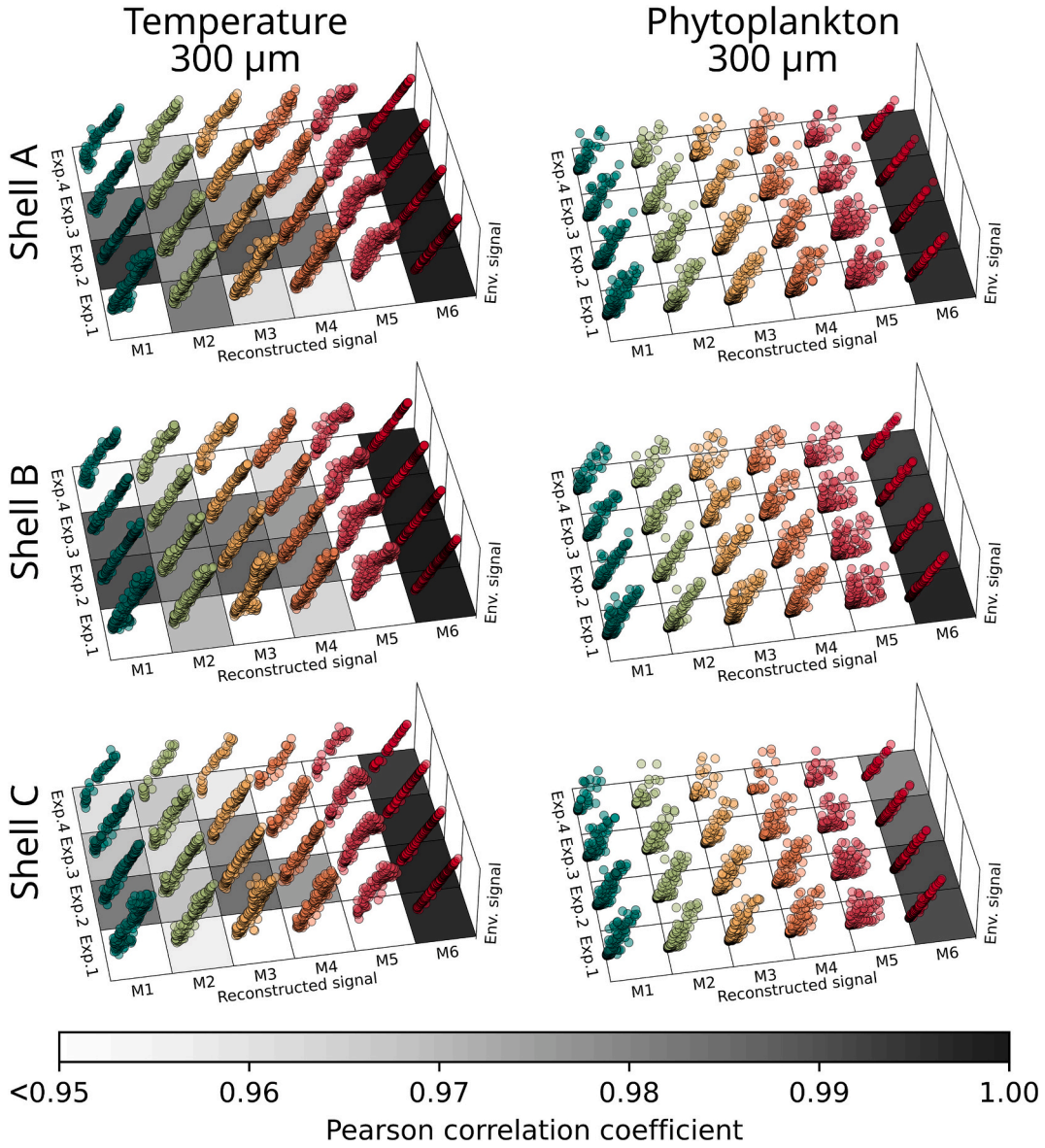

Fig. 3. Reconstruction accuracies of the digital sampling experiments using 300 µm wide sample spots. The correlation plots are calculated between the reconstructed signals and the underlying synthetic environmental signals, i.e., the sea surface temperature (left) and phytoplankton abundance (right) for the three different digital shell models (Shell A, Shell B and Shell C). Each subplot shows the correlation of a specific sampling experiment (Exp. 1 to 4) in combination with one of the six different temporal alignment methods (M1 to M6). The color-coded patch below each individual experiment denotes the Pearson correlation coefficient of the respective experiment, i.e., darker colors indicate stronger correlations (all values are provided in the Supporting Information Fig. S9).

value can be approximated. Finally, the use of the seasonal growth model allows to convert the %gr into absolute calendar dates and therefore time dependent weight distributions can be approximated.

3. Results

3.1. Accuracy of sampling and alignment strategies

All experiments and temporal alignment strategies resulted in generally high degrees of correlations between the synthetic environmental data and the reconstructed signals (Figs. 3, 4 and Supporting Information Fig. S9, S10), with a mean Pearson correlation coefficient of 0.89 ± 0.08 (1σ). On average, SST signal reconstructions provided better correlations than the reconstructions of the phytoplankton signal, i.e., $r = 0.96$ and 0.82, respectively. Comparing the two different spot sizes revealed slightly lower average correlations for 300 µm spots ($r = 0.88$) than for 80 µm spots ($r = 0.90$). All sampling strategies showed relatively similar results with Exp. 2 being the highest correlation ($r = 0.91$), followed by Exp. 1 ($r = 0.90$) and Exp. 3 ($r = 0.89$) and finally, Exp. 4 with the lowest correlation coefficient of 0.85. M6 was the most accurate temporal alignment method, with an average Pearson correlation coefficient of 0.99 ± 0.01 (1σ). Both, alignment methods (M1 and M2) resulted in correlations of 0.93 followed by M3 and M4 with 0.91 and 0.87, respectively. The least accurate reconstructions were obtained using alignment method M5 with a Pearson correlation of 0.70 ± 0.20 (1σ). Assessing the differences among sampling strategies with respect to alignment methods (Table 2) demonstrated that sampling techniques of Exp. 2 resulted in the most accurate reconstructions in combination with M1, M2, M3, M4 and M6. Only alignment method M5 performed best in combination with sampling strategy of Exp. 4.

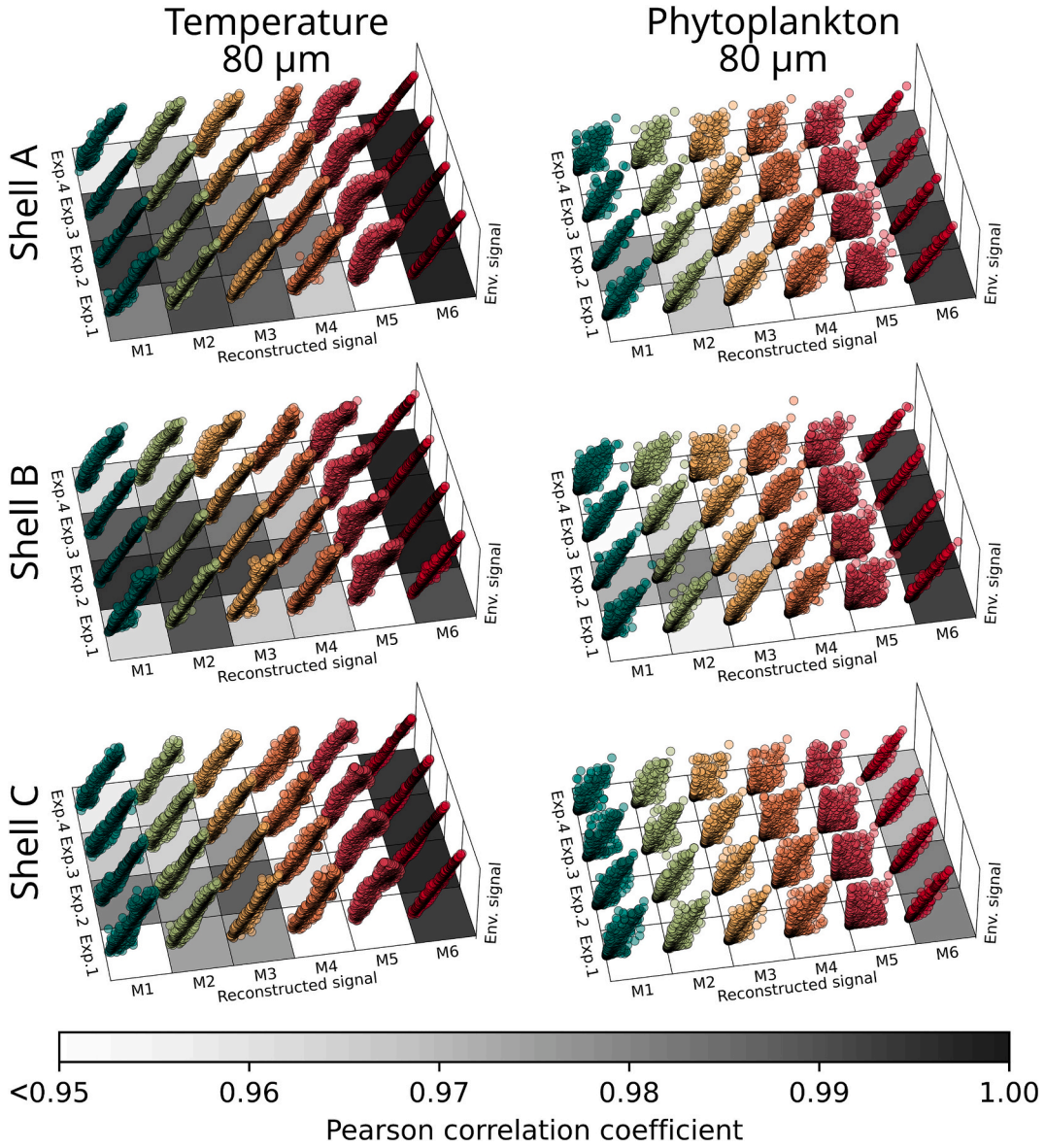

Fig. 4. Reconstruction accuracies of the digital sampling experiments using 80 µm wide sample spots. The correlation plots are calculated between the reconstructed signals and the underlying synthetic environmental signals, i.e., the sea surface temperature (left) and phytoplankton abundance (right) for the three different digital shell models (Shell A, Shell B and Shell C). Each subplot shows the correlation of a specific sampling experiment (Exp. 1 to 4) in combination with one of the six different temporal alignment methods (M1 to M6). The color-coded patch below each individual experiment denotes the Pearson correlation coefficient of the respective experiment, i.e., darker colors indicate stronger correlations (all values are provided in the Supporting Information Fig. S10).

Table 2
Averaged Pearson correlation coefficients calculated between the reconstructed signals and the underlying environmental signals (SST and phytoplankton abundance) for all digital experiments (Exp. 1 to Exp. 4) and alignment methods (M1 to M6).

	M1	M2	M3	M4	M5	M6
Exp. 1	0.93	**0.95**	0.93	0.90	0.68	0.99
Exp. 2	**0.96**	**0.95**	**0.96**	**0.92**	0.68	**1.00**
Exp. 3	0.94	0.94	0.94	0.86	0.69	0.99
Exp. 4	0.88	0.88	0.81	0.81	**0.74**	0.99

4. Discussion

4.1. Sampling strategies

The sampling strategies tested in this study (Exp. 1 to 4) provided generally high degrees of correlations between the synthetic environmental data and the reconstructed signals (Figs. 3 and 4). Nevertheless, small differences in the resulting accuracies existed among the sampling techniques. The results demonstrate that placing the sample spots within growth increments, i.e., without intersecting annual growth lines and parallel to the shell surface (Exp. 2), generated the most accurate reconstructions. This is because sampling tracks placed along the outer portion of the OSL (Fig. 2B; Track 2) allow to fit more samples into an increment resulting in a higher temporal resolution (i.e., lower time-averaging) compared to Exp. 3 and 4. Moreover, avoiding spots intersecting annual growth lines enhances the precision of the alignment, because slowly growing shell portions, like those that are close to annual growth lines, result in largely time-averaged signals. A problem that has received little attention in the sclerochronological literature is temporal overlap of samples even if they do not overlap spatially (Fig. 1), introducing reconstruction biases. Using the digital shells, it was possible to calculate the similarity of a sample spot with its preceding sample spot (Supporting Information Fig. S11). Interestingly, the experiments showed (Supporting Information Fig. S12) that samples can share more than 50 % of the (geochemical) information with a previous sample, especially during times of faster shell growth, which in turn is determined by the seasonal growth model. However, these similarities differed among sampling strategies. When positioning samples following Exp. 1 and 2, spots will largely overlap. By increasing the angle of the sampling track relative to the outer shell surface (Exp. 3 and 4), the extent of overlap can be minimized (Supporting Information Fig. S12). Those overlaps are controlled by the increment morphology, the distance between individual samples and the spot diameter, which also influence the temporal resolution. Conclusively, the average accuracy of reconstructed signals was highest for the Exp. 2 caused by more samples per increment but coincided with larger temporal overlaps. These temporal overlaps should be carefully considered in geochemical analyses by adjusting the sampling technique as well as the temporal alignment method (see Section 4.2.).

4.2. Temporal alignment methods

While the sampling strategies yielded closely similar correlation coefficients (Section 4.1), the alignment method comparison revealed larger differences. Therefore, the accuracy of reconstructed geochemical chronologies suggests to be mostly influenced by the temporal alignment method rather than the sampling strategy. On average, all tested alignment methods (Fig. 2C) demonstrably resulted in high correlations between the reconstructed and the environmental signal (Figs. 3 and 4), indicating all methods appear to be applicable to align geochemical data (Supporting Information Fig. S13 and S14). If the analysis aims to accurately reconstruct sub-seasonal signals, a careful selection of the alignment method becomes crucial. One significant step toward improving the alignment techniques is the approximation of the temporal ranges covered by individual sample spots (i.e., M5 and M6). Yet, appropriate reconstruction accuracies can be achieved using the temporal alignment M1 to M4, especially when the underlying signal is characterized by gradual, seasonal oscillations like the SST time-series rather than highly dynamic and abrupt changes (i.e., phytoplankton time-series). However, M1 to M4 associate the centroid of spots to single dates rather than ranges (Fig. 2C), which can result in strongly misaligned signals and produce biases. In contrast, the time encapsulated within samples was approximated by M5 but, interestingly, resulted in weaker reconstruction accuracies. This outcome suggests that projecting the distance between annual growth lines and sample spots onto a reference line (Fig. 2C) can produce biases in the temporal alignment. However, this influence may differ among bivalve species with different growth morphologies, i.e., the growth line shapes of the herein tested *A. islandica* shells may be more affected by this temporal alignment method compared to shapes of other taxa (e.g., *Serripes groenlandicus* for which this method was initially developed by Vihtakari et al., 2016). In addition, the temporal ranges (between the start and end time of sample spot) determined by M5 were used to calculate the average environmental signal within that time window. As the correlations were computed between the sample signals and those averaged environmental signals, the findings suggest that temporal ranges alone are insufficient to produce accurate high-resolution reconstructions. Temporal alignment method M6 produced by far the most accurate reconstructions (Fig. 3). This method linearly interpolated the growth morphology by following the shape of each increment. If the shape is known, the past ventral margins, i.e., previous growth fronts, can be reconstructed for each time step during growth. Along with the spot perimeter, temporally constrained weight distributions can be approximated allowing to mathematically treat temporally overlapping samples. Moreover, M6 appeared to be a robust alignment method showing consistently high correlations, irrespective of the used sampling strategy.

4.3. Methodological reflections

To obtain realistic data, the digital shell models were mathematically reconstructed using empirical data. However, the underlying rules, such as logarithmic shell growth (Ubukata, 2001), simplify the complex and chaotic nature of growth and variable environmental conditions affecting shell morphology (Schöne, 2013). The growth was modeled using a defined seasonal growth model allowing no deviations, despite reported inter-annual differences (Höche et al., 2022; Schöne et al., 2022b). A homogenous distribution of geochemical signals within individual microgrowth increments was assumed although small geochemical heterogeneities may occur among contemporaneously formed shell material, e.g., due to microstructural differences between sub-layers of the bivalve shell (Brosset et al., 2022; Shirai et al., 2014). The impact of these uncertainties on temporal alignment accuracy needs further research. However, we assume that chaotic perturbations would equally affect the reconstruction accuracy of all alignment methods and, thus, our conclusion that M6 is a robust method may remain valid.

The increment shape and width – subject to change through ontogeny (Fig. 5A; Supporting Information Fig. S15) – influence the number of landmarks and helping lines considered in M6. Testing multiple configurations (Fig. 5B) demonstrated that for broad, curved increments, which can be typically observed in shell portions formed during early ontogeny, the number of helping lines is the dominant factor for accuracy. In contrast, for increments in ontogenetically older shell portions, characterized by longer growth lines and narrower increments, the number of landmarks significantly impacts alignment results (Fig. 5C). Therefore, M6 could have achieved even higher accuracies if more helping lines were considered within the numerical simulations.

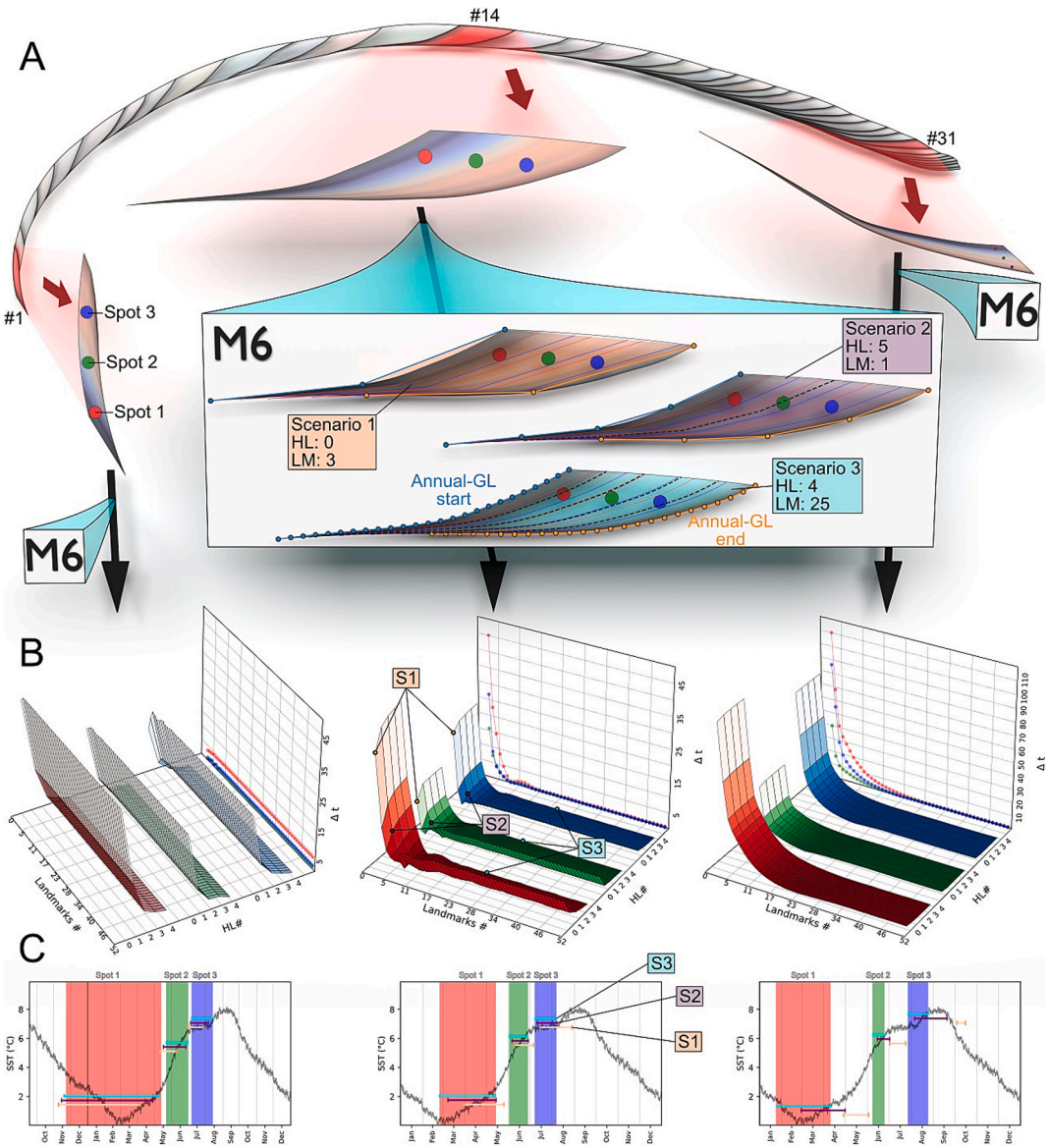

Fig. 5. Temporal alignment method M6 applied on three sample spots (Spot 1, 2 and 3) positioned in ontogenetically different growth increments, i.e., year 1, 14 and 31 (A). As the accuracy of this method is influenced by the number of helping lines (HL) and the number of landmarks (LM) that were used, different configurations that were tested, with three different scenarios (S1, S2, S3) on increment #14 exemplarily depicted in the center box in A. The temporal difference (Δt) between the reconstructed ranges and the true ranges was determined by calculating the square root of the sum of the squared differences between the start and end time. The effect of landmark and helping line number on Δt for all three sample spots are shown in B. Reconstructed ranges for Spot 1, 2 and 3 according to scenarios S1 (orange), S2 (purple) and S3 (cyan) indicated as horizontal lines (C). Note that for a clearer representation a small offset along the y-axis was added to the samples. Ranges that are covered by each sample are indicated as vertical color-coded bars. (For interpretation of the references to color in this figure legend, the reader is referred to the web version of this article.)

4.4. *Modeling geochemical profiles – an outlook*

The main purpose of developing M6 was to improve the high-resolution reconstruction of dynamic paleoenvironmental signals, e.g., phytoplankton blooms (e.g., Thébault et al., 2022). In this context, the approximations of temporally constrained weights can provide useful information. Specifically, the timing and magnitude of phytoplankton blooms, as recorded in geochemical profiles (e.g., Poitevin et al., 2022), can be modeled using time-averaged samples and corresponding weights (Fig. 6). Since the phenology of a plankton bloom can be described by Gaussian functions (Zhai et al., 2012), a numerical optimization algorithm (e.g., L-BFGS-B) can be used to identify the best fit by minimizing the sum of least squares between weighted and predicted values. This approach can be complemented by a Monte Carlo process that iteratively tests randomly selected initial parameters. This approach was tested on Shell A for different increments and spot sizes. As expected, the measured, raw signals tend to underestimate the peak magnitudes due to time-averaging effects (Fig. 6A). However, the fitted models differ from the time-series produced by the sample ranges (Fig. 6B) and showed remarkable similarities to the underlying environmental signals (Fig. 6C). Applying this modeling approach with the previously proposed method (M6) offers a promising opportunity to accurately reconstruct the absolute height and timing of the peaks, potentially enabling a reliable reconstruction of past phytoplankton dynamics.

5. Conclusion

This study systematically tested the influence of different sclerochronological sampling strategies as well as temporal alignment

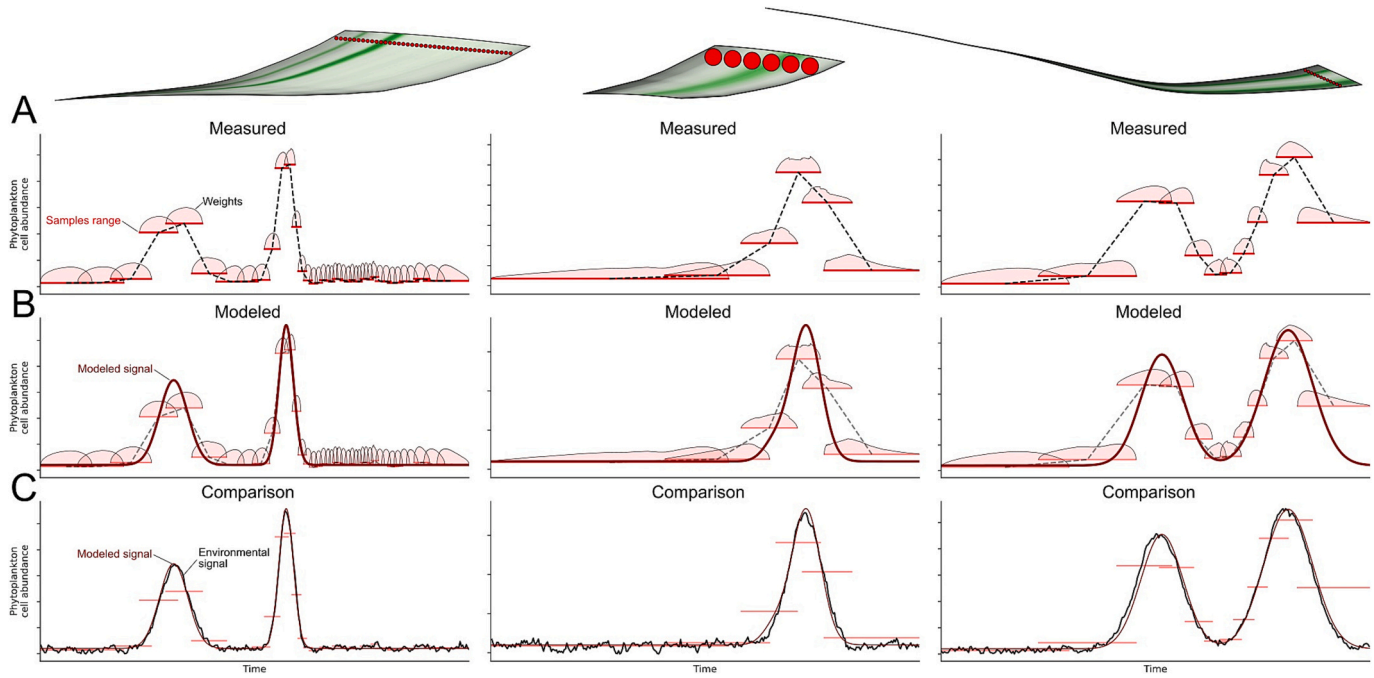

Fig. 6. Exemplary reconstruction of the underlying phytoplankton signal based on sample spots taken from three increments (left to right). The color intensities within the growth increments correspond to the signal archived in the microgrowth increments (A). Red circles indicate the sample spot positions and diameter, i.e., 80 µm (left and right) and 300 µm (center). Temporal ranges of sample spots shown as horizontal, red lines with corresponding weight distribution, as approximated by alignment method M6. The underlying signal, as modeled on the basis of Gaussian functions using numerical optimization algorithms and the approximated sample weights, represented as darkred curves (B). Comparison of modeled to environmental signal is shown in C. (For interpretation of the references to color in this figure legend, the reader is referred to the web version of this article.)

methods on the fidelity of high-resolution reconstructions of geochemical signals encoded in incrementally growing biogenic archives. This was achieved by employing digital models of cross-sections that were empirically constructed from *A. islandica* shells with synthetically generated environmental signals. The discretization of the continuous process of shell formation into numerous, extremely small microgrowth steps allowed the evaluation of how different alignment methods affect the temporal contextualization of geochemical data. Numerical simulations underscored the critical role of both sampling strategies and alignment methods in enhancing the reliability of paleoenvironmental reconstructions. Specifically, placing sample spots parallel to the shell surface without intersecting annual growth lines demonstrably resulted in the most accurate sampling strategy in combination with most alignment techniques. In comparison to conventional methods, the new temporal alignment method significantly improved the accuracy. This improvement was achieved because the sample spot geometry, the shape of growth lines and the increment morphology was considered within this temporal alignment approach. An artifact of high-resolution geochemical sampling is that sample spots can temporally overlap, as demonstrated by the numerical simulations. The new alignment method can account for these overlaps because all time slices that are encompassed by individual samples can be approximated. Furthermore, temporally constrained weights, as approximated by the alignment method, allowed highly accurate reconstructions of dynamic events such as phytoplankton blooms. Although the method was exemplarily demonstrated on shells of *A. islandica*, the underlying principles and methods developed in this study are not limited to this species but broadly applicable for a wide range of high-resolution biogeochemical archives.

CRediT authorship contribution statement

Lukas Fröhlich: Writing – original draft, Visualization, Software, Methodology, Formal analysis, Data curation, Conceptualization. **Qian Huang:** Writing – original draft, Validation, Investigation, Data curation, Conceptualization. **Bernd R. Schöne:** Writing – review & editing, Supervision, Resources, Project administration, Funding acquisition.

Declaration of competing interest

The authors declare that they have no known competing financial interests or personal relationships that could have appeared to influence the work reported in this paper.

Data availability

Data will be made available on request.

Acknowledgements

This project has received funding from the European Research Council (ERC) under the European Union's Horizon 2020 Research and Innovation Program (grant agreement No 856488—ERC Synergy project "SEACHANGE: Quantifying the impact of major cultural transitions on marine ecosystem functioning and biodiversity").

Appendix A. Supplementary data

Supplementary data to this article can be found online at https://doi.org/10.1016/j.palaeo.2025.113003.

References

Brosset, C., Höche, N., Shirai, K., Nishida, K., Mertz-Kraus, R., Schöne, B.R., 2022. Strong coupling between biomineral morphology and Sr/Ca of *Arctica islandica* (Bivalvia) - Implications for shell Sr/Ca-based temperature estimates. Minerals 12, 500. https://doi.org/10.3390/MIN12050500.

Butler, P.G, Wanamaker, A.D., Scourse, J.D., Richardson, C.A., Reynolds, D.J., 2013. Variability of marine climate on the North Icelandic Shelf in a 1357-year proxy archive based on growth increments in the bivalve *Arctica islandica*. Palaeogeogr.

Palaeoclimatol. Palaeoecol. 373, 141–151. https://doi.org/10.1016/j.palaeo.2012.01.016.
Doré, J., Chaillou, G., Poitevin, P., Lazure, P., Poirier, A., Chauvaud, L., Archambault, P., Thébault, J., 2020. Assessment of Ba/Ca in *Arctica islandica* shells as a proxy for phytoplankton dynamics in the Northwestern Atlantic Ocean. Estuar. Coast. Shelf Sci. 237, 106628. https://doi.org/10.1016/j.ecss.2020.106628.
Fröhlich, L., Siebert, V., Huang, Q., Thébault, J., Jochum, K.P., Schöne, B.R., 2022. Deciphering the potential of Ba/Ca, Mo/Ca and Li/Ca profiles in the bivalve shell *Pecten maximus* as proxies for the reconstruction of phytoplankton dynamics. Ecol. Indic. 141, 109121. https://doi.org/10.1016/j.ecolind.2022.109121.
Fröhlich, L., Siebert, V., Huang, Q., Thébault, J., Moriceau, B., Jochum, K.P., Schöne, B. R., 2023. Uptake of barium, molybdenum, and lithium and incorporation into scallop shells: refining proxies for primary production dynamics. Limnol. Oceanogr. 9999, 1–18. https://doi.org/10.1002/LNO.12440.
Gillikin, D.P., Lorrain, A., Paulet, Y.M., André, L., Dehairs, F., 2008. Synchronous barium peaks in high-resolution profiles of calcite and aragonite marine bivalve shells. Geo-Mar. Lett. 28, 351–358. https://doi.org/10.1007/s00367-008-0111-9.
Goodwin, D.H., Flessa, K.W., Schöne, B.R., Dettman, D.L., 2001. Cross-calibration of daily growth increments, stable isotope variation, and temperature in the Gulf of California bivalve mollusk *Chione cortezi*: implications for paleoenvironmental analysis. Palaios 16, 387–398. https://doi.org/10.1669/0883-1351(2001)016<0387:CCODGI>2.0.CO;2.
Goodwin, D.H., Schöne, B.R., Dettman, D.L., 2003. Resolution and fidelity of oxygen isotopes as paleotemperature proxies in bivalve mollusk shells: models and observations. Palaios 18, 110–125. https://doi.org/10.1669/0883-1351(2003)18<110:RAFOOI>2.0.CO;2.
Hanna, E., Jónsson, T., Ólafsson, J., Valdimarsson, H., 2006. Icelandic coastal sea surface temperature records constructed: Putting the pulse on air–sea–climate interactions in the northern North Atlantic. Part I: Comparison with HadISST1 open-ocean surface temperatures and preliminary analysis of long-term patterns and anomalies of SSTs around Iceland. J. Climate 19, 5652–5666. https://doi.org/10.1175/JCLI3933.1.
Höche, N., Walliser, E.O., Schöne, B.R., 2022. Microstructural mapping of *Arctica islandica* shells reveals environmental and physiological controls on biomineral size. Front. Earth Sci. 9, 1–19. https://doi.org/10.3389/feart.2021.781305.
Höche, N., Zettler, M.L., Huang, X., Schöne, B.R., 2023. Shell microstructures (disturbance lines) of *Arctica islandica* (Bivalvia): a potential proxy for severe oxygen depletion. Front. Mar. Sci. 10. https://doi.org/10.3389/fmars.2023.1219716.
Jolivet, A., Asplin, L., Strand, O., Thebault, J., Chauvaud, L., 2015. Coastal upwelling in Norway recorded in Great Scallop shells. Limnol. Oceanogr. 60, 1265–1275. https://doi.org/10.1002/LNO.10093.
Jones, D.S., 1980. Annual cycle of shell growth increment formation in two continental shelf bivalves and its paleoecologic significance. Paleobiology 3, 331–340. https://doi.org/10.1017/S0094837300006837.
Jones, D.S., Quitmyer, I.R., 1996. Marking time with bivalve shells: oxygen isotopes and season of annual increment formation. Palaios 11, 340–346. https://doi.org/10.2307/3515244.
Marali, S., Schöne, B.R., 2015. Oceanographic control on shell growth of *Arctica islandica* (Bivalvia) in surface waters of Northeast Iceland — Implications for paleoclimate reconstructions. Palaeogeogr. Palaeoclimatol. Palaeoecol. 420, 138–149. https://doi.org/10.1016/J.PALAEO.2014.12.016.
Marali, S., Schöne, B.R., Mertz-Kraus, R., Griffin, S.M., Wanamaker, A.D., Matras, U., Butler, P.G., 2017. Ba/Ca ratios in shells of *Arctica islandica*—Potential environmental proxy and crossdating tool. Palaeogeogr. Palaeoclimatol. Palaeoecol. 465, 347–361. https://doi.org/10.1016/j.palaeo.2015.12.018.
Marchitto, T.M., Jones, G.A., Goodfriend, G.A., Weidman, C.R., 2000. Precise temporal correlation of Holocene mollusk shells using sclerochronology. Quaternary Res. 53, 236–246. https://doi.org/10.1006/qres.1999.2107.
Peharda, M., Schöne, B.R., Black, B.A., Corrège, T., 2021. Advances of sclerochronology research in the last decade. Palaeogeogr. Palaeoclimatol. Palaeoecol. 570, 110371. https://doi.org/10.1016/J.PALAEO.2021.110371.
Poitevin, P., Roy, V., Galbraith, P.S., Chaillou, G., 2022. Insights into coastal phytoplankton variations from 1979 to 2018 derived from Ba/Ca records in scallop shells (*Chlamys islandica*) from a fishing ground in the northern Gulf of St. Lawrence. Mar. Environ. Res. 181, 105734. https://doi.org/10.1016/J.MARENVRES.2022.105734.
Reynolds, D.J., von Biela, V.R., Dunton, K.H., Douglas, D.C., Black, B.A., 2022. Sclerochronological records of environmental variability and bivalve growth in the Pacific Arctic. Prog. Oceanogr. 206, 102864. https://doi.org/10.1016/J.POCEAN.2022.102864.
Schöne, B.R., 2013. *Arctica islandica* (Bivalvia): A unique paleoenvironmental archive of the northern North Atlantic Ocean. Glob Planet Change 111, 199–225. https://doi.org/10.1016/j.gloplacha.2013.09.013.
Schöne, B.R., Huang, Q., 2021. Ontogenetic $\delta^{15}N$ trends and multidecadal variability in shells of the bivalve mollusk,. *Arctica islandica.* 8, 1–15. https://doi.org/10.3389/fmars.2021.748593.
Schöne, B.R., Dunca, E., Fiebig, J., Pfeiffer, M., 2005. Mutvei's solution: An ideal agent for resolving microgrowth structures of biogenic carbonates. Palaeogeogr. Palaeoclimatol. Palaeoecol. 228, 149–166. https://doi.org/10.1016/J.PALAEO.2005.03.054.
Schöne, B.R., Huang, X., Jantschke, A., Mertz-Kraus, R., Zettler, M.L., Liu, D., Yu, K., 2022a. High-Resolution reconstruction of dissolved oxygen levels in the Baltic Sea with bivalves: a multi-species comparison (Arctica islandica, Astarte borealis, Astarte elliptica). 9, 820731. https://doi.org/10.3389/fmars.2022.820731.
Schöne, B.R., Marali, S., Mertz-kraus, R., Butler, P.G., Wanamaker, A.D., Fröhlich, L., 2022b. Importance of weighting high-resolution proxy data from bivalve shells to avoid bias caused by sample spot geometry and variability in seasonal growth rate. Front. Earth Sci. 10, 1–17. https://doi.org/10.3389/feart.2022.889115.
Schöne, B.R., Marali, S., Jantschke, A., Mertz-Kraus, R., Butler, P.G., Fröhlich, L., 2023. Can element chemical impurities in aragonitic shells of marine bivalves serve as proxies for environmental variability? Chem. Geol. 616, 121215. https://doi.org/10.1016/J.CHEMGEO.2022.121215.
Shirai, K., Schöne, B.R., Miyaji, T., Radarmacher, P., Krause, R.A., Tanabe, K., 2014. Assessment of the mechanism of elemental incorporation into bivalve shells (*Arctica islandica*) based on elemental distribution at the microstructural scale. Geochim. Cosmochim. Acta 126, 307–320. https://doi.org/10.1016/J.GCA.2013.10.050.
Smith, T., Zotta, R.M., Boulton, C.A., Lenton, T.M., Dorigo, W., Boers, N., 2023. Reliability of resilience estimation based on multi-instrument time series. Earth Syst. Dynam. 14, 173–183. https://doi.org/10.5194/esd-14-173-2023.
Thébault, J., Schöne, B.R., Hallmann, N., Barth, M., Nunn, E.V., 2009. Investigation of Li/Ca variations in aragonitic shells of the ocean quahog *Arctica islandica*, northeast Iceland. Geochem. Geophys. Geosyst. 10, Q12008. https://doi.org/10.1029/2009GC002789.
Thébault, J., Jolivet, A., Waeles, M., Tabouret, H., Sabarot, S., Pécheyran, C., Leynaert, A., Jochum, K.P., Schöne, B.R., Fröhlich, L., Siebert, V., Amice, E., Chauvaud, L., 2022. Scallop shells as geochemical archives of phytoplankton-related ecological processes in a temperate coastal ecosystem. Limnol. Oceanogr. 67, 187–202. https://doi.org/10.1002/lno.11985.
Trofimova, T., Andersson, C., Bonitz, F.G.W., Pedersen, L.E.R., Schöne, B.R., 2021. Reconstructing early Holocene seasonal bottom-water temperatures in the northern North Sea using stable oxygen isotope records of *Arctica islandica* shells. Palaeogeogr. Palaeoclimatol. Palaeoecol. 567, 110242. https://doi.org/10.1016/j.palaeo.2021.110242.
Tzadik, O.E., Curtis, J.S., Granneman, J.E., Kurth, B.N., Pusack, T.J., Wallace, A.A., Hollander, D.J., Peebles, E.B., Stallings, C.D., 2017. Chemical archives in fishes beyond otoliths: A review on the use of other body parts as chronological recorders of microchemical constituents for expanding interpretations of environmental, ecological, and life-history changes. Limnol. Oceanogr. Methods 15, 238–263. https://doi.org/10.1002/LOM3.10153.
Ubukata, T., 2001. Stacking increments: A new model and morphospace for the analysis of bivalve shell growth. Hist. Biol. 15, 303–321. https://doi.org/10.1080/08912960210000244475.
Vihtakari, M., Renaud, P.E., Clarke, L.J., Whitehouse, M.J., Hop, H., Carroll, M.L., Ambrose, W.G., 2016. Decoding the oxygen isotope signal for seasonal growth patterns in Arctic bivalves. Palaeogeogr. Palaeoclimatol. Palaeoecol. 446, 263–283. https://doi.org/10.1016/J.PALAEO.2016.01.008.
Wanamaker, A.D., Heinemeier, J., Scourse, J.D., Richardson, C.A., Butler, P.G., Eiríksson, J., Knudsen, K.L., 2008. Very long-lived mollusks confirm 17th century AD tephra-based radiocarbon reservoir ages for North Icelandic shelf waters. Radiocarbon 50, 399–412. https://doi.org/10.1017/S0033822200053510.
Weidman, C.R., Jones, G.A., Kyger, 1994. The long-lived mollusc *Arctica islandica*: A new paleoceanographic tool for the reconstruction of bottom temperatures for the continental shelves of the northern North Atlantic Ocean. J. Geophys. Res. 99, 18305-18314. https://doi.org/10.1029/94jc01882.
Zhai, L., Gudmundsson, K., Miller, P., Peng, W., Gufinnsson, H., Debes, H., Hátún, H., White, G.N., Walls, R.H., Sathyendranath, S., Platt, T., 2012. Phytoplankton phenology and production around Iceland and Faroes. Cont. Shelf Res. 37, 15–25. https://doi.org/10.1016/j.csr.2012.01.013.